APPLIED PHYSICS LETTERS **105**, 023104 (2014)

Air damping of atomically thin MoS_2 nanomechanical resonators

Jaesung Lee,[1] Zenghui Wang,[1] Keliang He,[2] Jie Shan,[2] and Philip X.-L. Feng[1,a)]
[1]*Department of Electrical Engineering and Computer Science, Case School of Engineering, Case Western Reserve University, 10900 Euclid Avenue, Cleveland, Ohio 44106, USA*
[2]*Department of Physics, College of Arts and Sciences, Case Western Reserve University, 10900 Euclid Avenue, Cleveland, Ohio 44106, USA*

(Received 10 May 2014; accepted 4 July 2014; published online 15 July 2014)

We report on experimental measurement of air damping effects in high frequency nanomembrane resonators made of atomically thin molybdenum disulfide (MoS_2) drumhead structures. Circular MoS_2 nanomembranes with thickness of monolayer, few-layer, and multi-layer up to ~70 nm (~100 layers) exhibit intriguing pressure dependence of resonance characteristics. In completely covered drumheads, where there is no immediate equilibrium between the drum cavity and environment, resonance frequencies and quality (Q) factors strongly depend on environmental pressure due to bulging of the nanomembranes. In incompletely covered drumheads, strong frequency shifts due to compressing-cavity stiffening occur above ~200 Torr. The pressure-dependent Q factors are limited by free molecule flow (FMF) damping, and all the mono-, bi-, and tri-layer devices exhibit lower FMF damping than thicker, conventional devices do. © *2014 AIP Publishing LLC*. [http://dx.doi.org/10.1063/1.4890387]

Two-dimensional (2D) crystals, such as graphene and molybdenum disulfide (MoS_2), have recently been enabling a new class of atomically thin nanoelectromechanical systems (NEMS) for sensing and actuation functions.[1–6] Due to their ultimately small motional masses yet large capture areas, 2D NEMS offer promises for ultrasensitive detection of physical quantities (force, temperature, adsorbed mass, charge, etc.) based on resonance frequency shift, and for tunable electromechanical signal generation and processing in ultralow-power 2D crystal platforms.[4] In these resonant transducers, quality (Q) factors of their resonances are key to the device performance and sensitivity: higher Q allows finer frequency shifts be resolved, which increases the sensitivity and resolution. As high-Q devices are desired in these scenarios, probing the origins of energy dissipation (Q^{-1}) and limits of damping processes in these emerging 2D systems are needed.

Air damping, an energy loss pathway due to the interactions between the vibrating structure and surrounding air molecules, can be an important dissipation mechanism when devices are operated in moderate vacuum or near ambient. Beyond pursuing highest possible Q's for the aforementioned applications in vacuum, in wider pressure ranges, quantifying pressure dependences and understanding air damping effects in 2D nanomechanical resonators can also be important for exploring new technological niches in applications such as nerve gas detection, pressure sensing, functionalized surfaces (e.g., "smart skins"), cochlear implants, ultrasonic transducers (for high-resolution imaging/position detection), and miniaturized microphones and speakers spanning wide acoustic bands.[7] To date, pressure dependences and air damping have been widely investigated in conventional resonant microelectromechanical systems (MEMS), such as in doubly clamped beams,[8–11] cantilevers,[11–14] torsional paddles,[15] and drumhead membrane[16] resonators, and in various mainstream structural materials (e.g., Si and SiN), demonstrating pressure (p) dependent dissipation processes, with $Q \sim p^{-1}$ and $Q \sim p^{-1/2}$ power laws, in different pressure ranges.[8–16]

While resonance characteristics of 2D NEMS resonators have been reported, only a few experiments have been conducted to study the dissipation processes such as temperature dependence of Q factors[2,3] and surface losses in 2D devices.[6] In addition, while resonance frequency shifts due to bulging of graphene membrane has been demonstrated with varying pressure,[17] air damping in such atomically thin NEMS has not yet been investigated. The simple power law pressure dependence of Q found in conventional 3D MEMS may not be directly applicable to 2D NEMS, as 2D devices' high surface-to-volume ratios, ultra-small movable masses, and high strain tunability may result in different air damping behaviors. In this work, we investigate air damping effects in drumhead MoS_2 resonators with different thicknesses (from mono-, bi-, tri-layer, to ~100 layers) and investigate the different types of interactions between the MoS_2 devices with air molecules, including pressure-induced bulging, free molecule flow (FMF) damping, and compressing-cavity stiffening, by measuring their resonance characteristics with varying pressure.

MoS_2 devices are fabricated by mechanical exfoliation as described before.[6] We use a modulated 405 nm laser for motion actuation.[18] It is focused ~5–10 μm apart from the device, with power <250 μW and an intentionally defocused spot size of ~5 μm to avoid excessive laser heating. A 633 nm laser is focused on the device (spot size ~1 μm) to read out the device motion,[6] with power < 350 μW to avoid parasitic heating. The chamber pressure p is varied from ~6 mTorr to atmosphere pressure (~760 Torr) at room temperature.

Figure 1 shows the resonance characteristics of a bilayer MoS_2 resonator (diameter $d = 1.8\ \mu$m). Figure 1(c) shows that resonance frequency f_{res} first decreases as p increases from 14 mTorr to 295 Torr and then increases with pressure.

a)Author to whom correspondence should be addressed. Electronic mail: philip.feng@case.edu

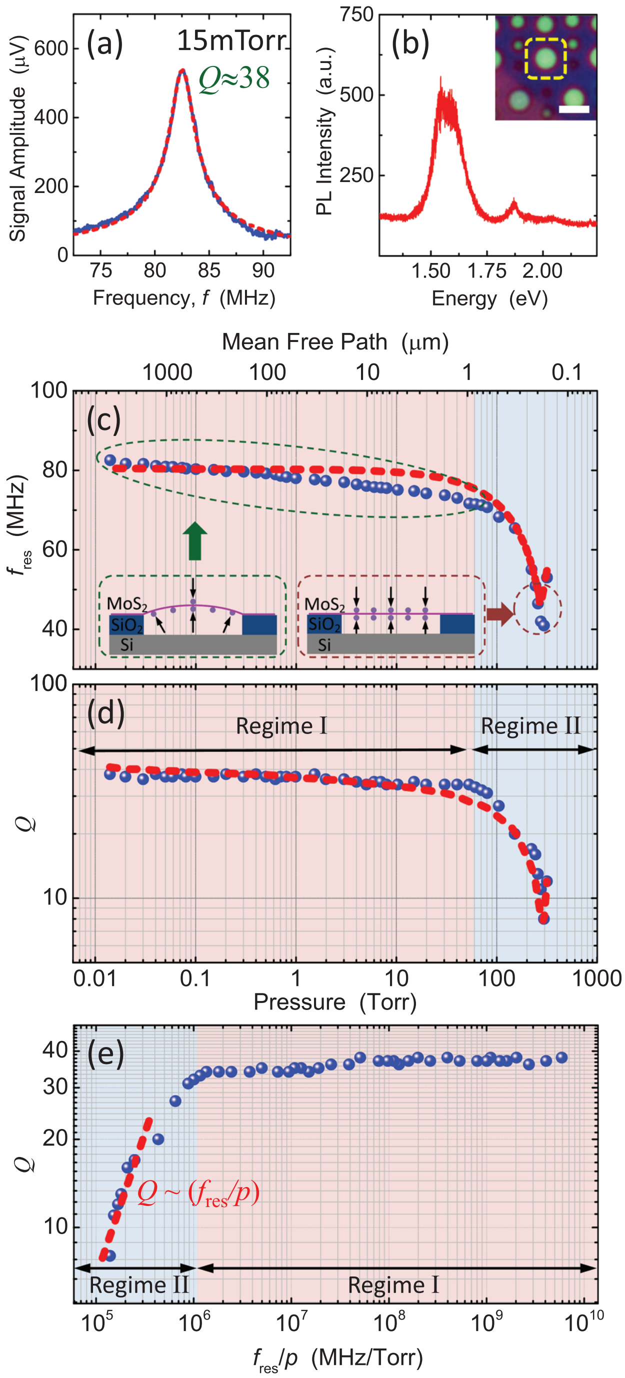

FIG. 1. Measured resonance characteristics from a completely covered bilayer MoS_2 resonator ($d = 1.8\,\mu$m). (a) Resonance at 15 mTorr. Red dashed line shows fitting to a damped harmonic resonator model.[6] (b) Photoluminescence (PL) data confirming bilayer MoS_2. *Inset*: optical image (scale bar: 2 μm). (c) f_{res} *vs.* p. Red dashed line shows the fitting using Eq. (1). *Inset*: schematics of device bulging. (d) Q *vs.* p. Red dashed line shows the fitting using Eq. (3). (e) Q as a function of f_{res}/p. In the FMF dominated region $Q \sim f_{res}/p$. (c)-(e): The light pink and light blue backgrounds represent different damping regimes where FMF is negligible and appreciable, respectively.

This is consistent with bulging induced tensioning of the membrane. As shown from the optical image, this device has no structural defects for air molecules to enter the microcavity sealed by the MoS_2 diaphragm, and thus the pressures inside and outside the cavity do not equilibrate on the experimental time scale. When the chamber is evacuated, the membrane inflates upward (i.e., bulging like a balloon) due to the pressure difference across the membrane, Δp, which is related to the deflection (δ) by[19]

$$\Delta p = \frac{4t\delta}{a^2}\left(\frac{\gamma}{t} + \frac{2}{3}\frac{\delta^2}{a^2}\frac{E_Y}{1.026 - 0.793\nu - 0.233\nu^2}\right), \quad (1)$$

where t, γ, a, E_Y, ν, and δ are the thickness, initial tension (in N/m), radius, Young's modulus, Poisson's ratio, and deflection (at the center) of the membrane, respectively. Here, we assume that the deflected membrane takes the form of a spherical cap, thus the bulging induced strain is $\Delta\varepsilon = \sqrt{A/A_0} - 1$, where A and A_0 are the total areas of the inflated and uninflated diaphragm. For a tensioned circular membrane, $f_{res} = 2.404(E_Y(\varepsilon_0 + \Delta\varepsilon)/\rho)^{1/2}/2\pi a$ for the fundamental mode (ρ: mass density; ε_0: initial strain), from which we calculate the f_{res}-Δp curve. We find very good agreement between theory and data (Fig. 1(c)), and the fitting indicates a constant residue pressure of $\sim$280 Torr inside the sealed cavity, which may result from air leaking out of the cavity very slowly as we store the device under moderate vacuum. We find $\delta \approx 22.3$ nm at the center of the membrane (giving an additional strain of $\Delta\varepsilon \approx 324$ ppm) at 15 mTorr, validating the assumption that the cavity volume (and thus the residue pressure inside) remains roughly constant throughout the experiment.

We further examine the pressure dependence of Q in this 2D resonator (Fig. 1(d)). We observe that as p increases, Q remains roughly constant up to $p \approx 60$ Torr (regime I), beyond which Q decreases with p (regime II), without exhibiting the common $Q \sim p^{-1}$ or $Q \sim p^{-1/2}$ power law found in conventional 3D MEMS resonators. This behavior is related to the 2D nature of our devices and is consistent with FMF damping.

FMF damping describes the energy loss process that a vibrating device strikes free air molecules and loses energy to them. The FMF-limited Q is[20]

$$Q_{FMF} = \frac{\rho t \omega_0}{4}\left(\frac{\pi RT}{2m}\right)^{1/2}\frac{1}{p}, \quad (2)$$

where $\omega_0 = 2\pi f_{res}$, T is the temperature, R is the gas constant, and m is the mass of gas molecule. Most conventional MEMS resonators (whose f_{res} values do not significantly vary with p) exhibit $Q \sim p^{-1}$ (as in Eq. (2)) in the pressure range where FMF damping dominates.

As p further increases, some MEMS resonators exhibit $Q \sim p^{-1/2}$, as viscous damping becomes dominant.[10,12,13] The ratio between the mean free path (MFP) of air molecules and the device dimension, defined as the Knudsen number, $\mathrm{Kn} = \lambda_{MFP}/l_{device}$, can be used to distinguish between these two damping regimes. Here, $\lambda_{MFP} = k_B T/(\sqrt{2}\pi\theta^2 p)$ is the MFP (k_B: Boltzmann constant, θ: air molecule diameter), and l_{device} is device characteristic length ($l_{device} = \sqrt{\pi a^2}$ for circular membrane, a: radius). When $Kn < 0.01$, viscous damping becomes significant.[21] Throughout our experiment, $0.04 < Kn < 2900$, thus our devices are not in the viscous damping regime. We confirm this by plotting measured Q as a function of f_{res}/p (Fig. 1(e)). We clearly see that at low pressure (regime I) the air damping is not the dominant dissipation process (Q independent of p); above 60 Torr, $Q \sim (f_{res}/p)$ (regime II, slope $\approx$ 1), consistent with FMF damping (Eq. (2)).

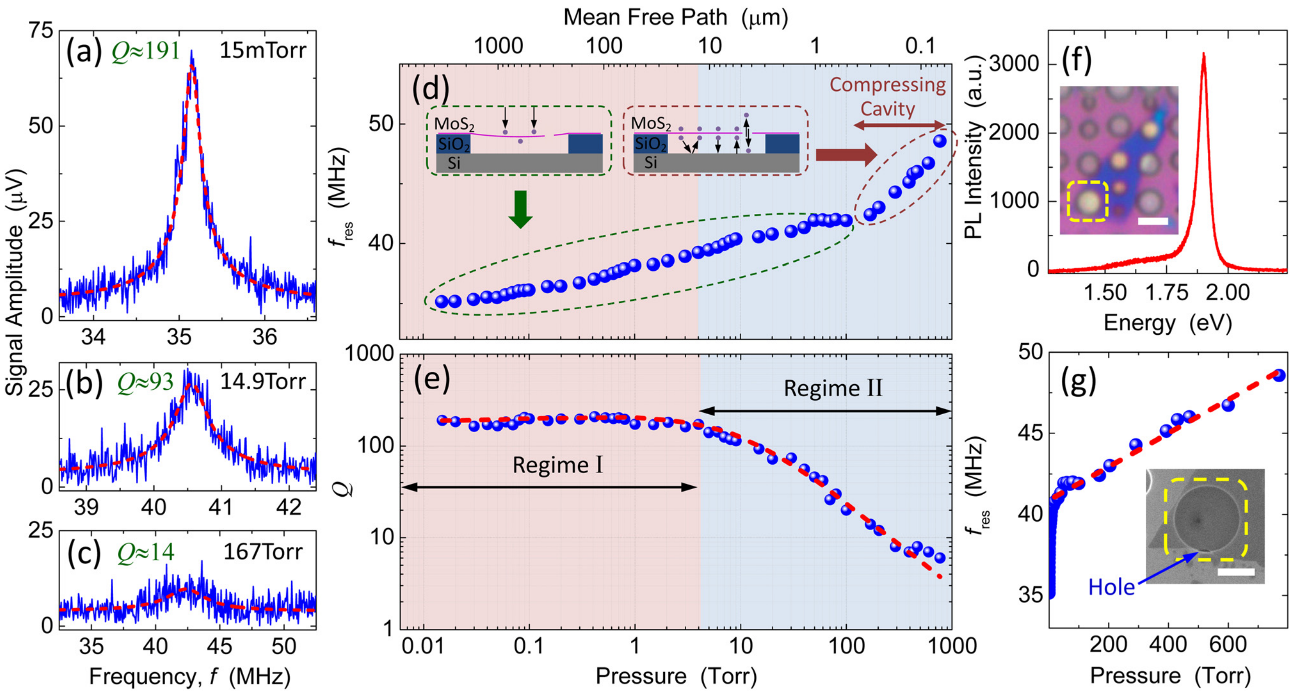

FIG. 2. Resonance characteristics for an incompletely covered monolayer MoS_2 resonator ($d = 1.8$ μm). (a)-(c) Measured resonances at 15 mTorr, 14.9 Torr, and 167 Torr, respectively. (d) Measured f_{res} *vs.* p. *Insets*: schematic illustration of pressurized depressing and compressing-cavity stiffening. (e) Q *vs.* p. Red dashed line shows the fitting using Eq. (3). Background color coding in (d) and (e): same as in Fig. 1. (f) Measured PL confirming monolayer MoS_2. *Inset*: optical microscope image (scale bar: 2 μm). (g) f_{res} *vs.* p in the linear scale, showing the expected $f_{res} \sim p$ relation in the compressing-cavity regime. *Inset*: SEM image (scale bar: 500 nm).

With FMF as the dominant p-dependent dissipation process, we have

$$(1/Q)_{Total} = (1/Q)_{p\text{-}indep} + \alpha(1/Q)_{FMF}, \tag{3}$$

where $Q^{-1}{}_{p\text{-}indep}$ describes all the dissipation processes independent of chamber pressure p, and α is a parameter related to device geometry and structural details. We find good agreement between Eq. (3) and measurement (Fig. 1(d)). Through fitting, we determine $\alpha \approx 0.125$ for this device.

One clear distinction of our 2D NEMS from conventional 3D devices is the absence of simple power law dependence in the Q-p relation. In 3D MEMS, where f_{res} depends little on pressure,[10–12,14] $Q \sim p^{-1}$ in the FMF regime, and at higher p, $Q \sim p^{-1/2}$ for viscous damping. In our 2D resonators, f_{res} shift significantly with p, hence Q does not simply follow the well-known $Q \sim p^{-1}$ or $Q \sim p^{-1/2}$ power law.

We further investigate air damping in a different category of devices, where MoS_2 flakes do not completely seal the microcavities underneath. This, in the appropriate environmental pressure regime, allows the pressure to equilibrate across the MoS_2 diaphragm. Figure 2 shows measurement of a $d = 1.8$ μm monolayer device with a small opening on the edge of the MoS_2 diaphragm (Fig. 2(g), inset). Throughout the experimental pressure range, f_{res} increases with p (Fig. 2(d)), most pronounced above 200 Torr. This is in striking contrast with the device in Fig. 1 (f_{res} decreases with p) and clearly different than most conventional 3D MEMS resonators (f_{res} changes little with p). This distinctive f_{res}-p behavior results from a combination of bulging induced tensioning and compressing-cavity stiffening.

Upon evacuating the chamber, the air inside the cavity leaks out. As the chamber gradually vents (less vacuum), at low pressure, the air molecules cannot effectively enter the cavity (even unsealed), because the MFP ($\lambda_{MFP} > 1$ μm) is much longer than the aperture size ($\sim 10^2$ nm), thus p inside cavity remains lower than outside. This causes the membrane to be depressed (Fig. 2(d), left inset), tensioning the membrane and increasing f_{res}. Once the chamber pressure rises to a point ($p \approx 200$ Torr) where the MFP becomes comparable to the opening (Fig. 2(d), top axis), the pressure values across the membrane become equilibrated, and compressing-cavity effect emerges to dominate the observed f_{res} variations.

The compressing-cavity effect we describe here is different than the known squeeze-film effect in conventional MEMS, because the MoS_2 drumhead cavities have impermeable vertical sidewalls, whereas classical squeeze-film effect is established in the air gap between a vibrating device and a nearby stationary surface where there is no sidewall and air can flow freely sideways.[16,22] In these 2D drumhead resonators, the possibility for squeeze-film effect to happen depends on the size of the leaking aperture (hole) (only holes big enough may allow efficient and instantaneous in-and-out squeezing of air). For a high f_{res} drumhead resonator with nanoscale hole, air molecules cannot escape the cavity fast enough while being compressed by the membrane's resonant motion. This compressing-cavity mechanism is manifested as an effective spring, causing stiffening of f_{res}. As the cavity pressure increases, the effective spring augments, enhancing the stiffening (Fig. 2(g), $p > 100$ Torr region).

Similar to the bilayer device (Fig. 1), we find again in the monolayer MoS_2 resonator (Fig. 2) that FMF damping

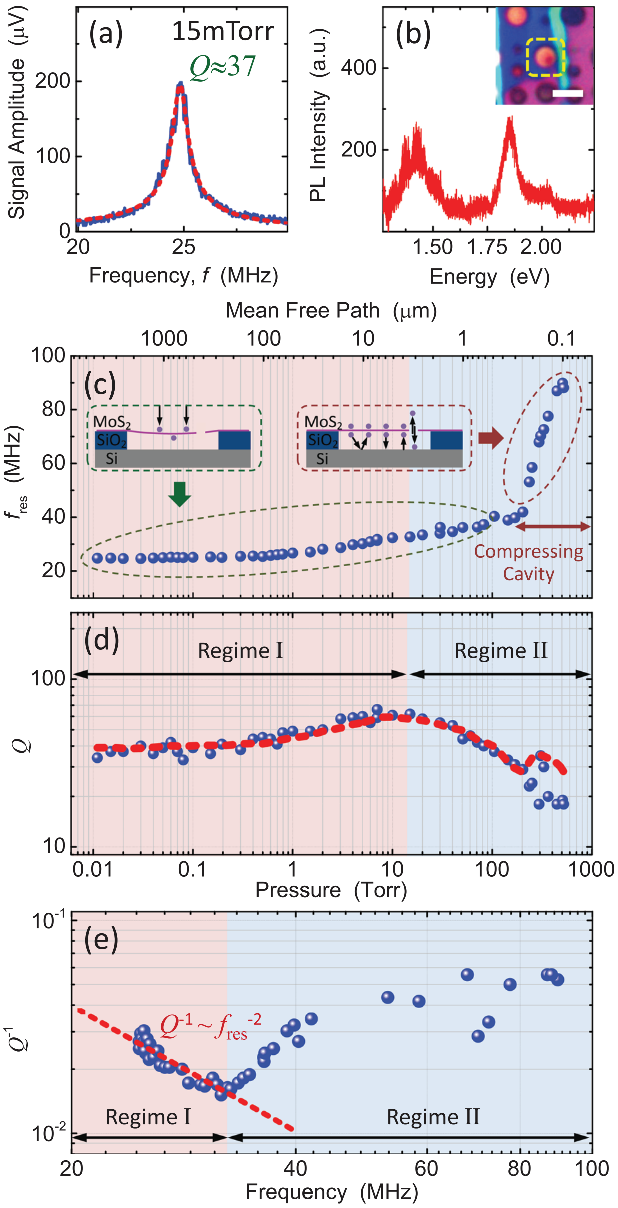

FIG. 3. Resonance characteristics of a trilayer MoS_2 resonator. (a) Resonance at 15 mTorr. (b) Measured PL confirming trilayer MoS_2. *Inset*: optical image (Scale bar: 2 μm). (c) Measured f_{res} *vs.* p. *Insets*: schematic illustration of pressurized depressing and compressing-cavity stiffening. (d) Q *vs.* p. Red dashed line shows the fitting using Eqs. (4) and (5). (e) Dissipation rate Q^{-1} as a function of f_{res}, with $Q^{-1} \sim f_{res}^{-2}$ observed in the low pressure regime (indicated by the red dashed line). Background color coding in (c)-(e): same as in Fig. 1.

is the dominant p-dependent damping mechanism (Fig. 2(e), regime II). Accordingly, our FMF-based calculation (Eq. (3)) produces good agreement with the measurement (Fig. 2(e)) and the fitting gives $\alpha \approx 0.25$ for this device. The 2-fold difference in α values reflects a subtle geometric effect: for the completely covered device in Fig. 1, the pressure inside the MoS_2-sealed cavity remains unchanged throughout the experiment; the amount of dissipation associated with the sealed air inside the cavity is thus independent of the pressure outside the cavity. Therefore, the observed p-dependence of Q originates only from the interaction of air molecules with the outer MoS_2 surface. In contrast, in the leaking device (Fig. 2), both sides of the MoS_2 membrane experience p-dependent air damping, thus its α coefficient is twice that of the other device (Fig. 1).

While the observed p-dependent behavior for 2D resonators (both closed and open geometries) agrees well with theories, we also discover resonance characteristics in MoS_2 NEMS beyond the existing nanomechanical theory framework. Figure 3 presents data from a trilayer MoS_2 resonator ($d = 1.8$ μm). Measured f_{res}-p curve (Fig. 3(c)) suggests the existence of a small opening. The Q-p data (Fig. 3(d)), however, shows distinctive behavior from the previous two devices: Q first increases with p (regime I) before the trend reverses (regime II).

To take a closer look at this unusual pressure dependence of Q, we plot Q^{-1} vs. f_{res} (Fig. 3(e)): within regime I, it exhibits a power law relation of $Q^{-1} \sim f_{res}^{-2}$. This suggests a dissipation mechanism in which the per-cycle energy loss is independent of f_{res}: as the energy stored in the resonator scales as f_{res}^2 (assuming other parameters unchanged), the Q factor (ratio of energy stored to per-cycle energy loss) exhibits f_{res}^2 dependence. We thus rewrite Eq. (3) as

$$(1/Q)_{Total} = (1/Q)_{non-FMF} + \alpha(1/Q)_{FMF}, \tag{4}$$

where

$$(1/Q)_{non-FMF} = \frac{f_{res}^{\ 2}|_{p\to 0}}{f_{res}^{\ 2}}(1/Q)|_{p\to 0} \tag{5}$$

reflects the $Q^{-1} \sim f_{res}^{-2}$ relation found in Fig. 3(e). Using Eqs. (2), (4), and (5), we find good agreement to the measurement (Fig. 3(d)). The fitting gives $\alpha \approx 0.25$, again confirming existence of leakage, similar to the device in Fig. 2.

We finally examine air damping in thicker devices. Figure 4 shows data from three $d \approx 5.6$ μm drumheads ($t \approx 13.6$ nm, 39.6 nm, and 68.1 nm). These thicker devices all exhibit robust mechanical resonances from vacuum to 1 atm, in contrast to the thinner devices, whose resonances become difficult to detect as p approaches atmosphere pressure (the highest pressure at which we obtain measurable resonances for the devices in Figs. 1–3 are $p \approx 316$, 770, and 520 Torr, respectively). Figure 4(c) shows that their f_{res} values remain mostly constant (like most 3D MEMS resonators) up to $p \approx 200$ Torr, beyond which compressing-cavity stiffening are observed (suggesting existence of leaking paths, whether visible or not in the device images). Less frequency shift is observed (for all p values): above 200 Torr, stiffening induced f_{res} increase ranges from 3%–21% (vs. 17%–130% in thinner devices). These observations are consistent with our previous findings:[6] the 1-, 2-, and 3-layer devices behave as membranes, whose f_{res} are much more susceptible to pressure. Figure 4(d) shows that all Q's decrease with p, most noticeably above 3 Torr. While data well matches the FMF-dominant equation (Eq. (2)), the extracted α values (0.7–1.7) are much larger than those found for the thinner devices, but close to those of conventional 3D MEMS ($\alpha \approx 1$). These observations show the transition from 2D to 3D, exemplifying the effect of dimensionality on air damping of NEMS devices.

In conclusion, air damping effects are experimentally demonstrated in 2D MoS_2 resonators with different device

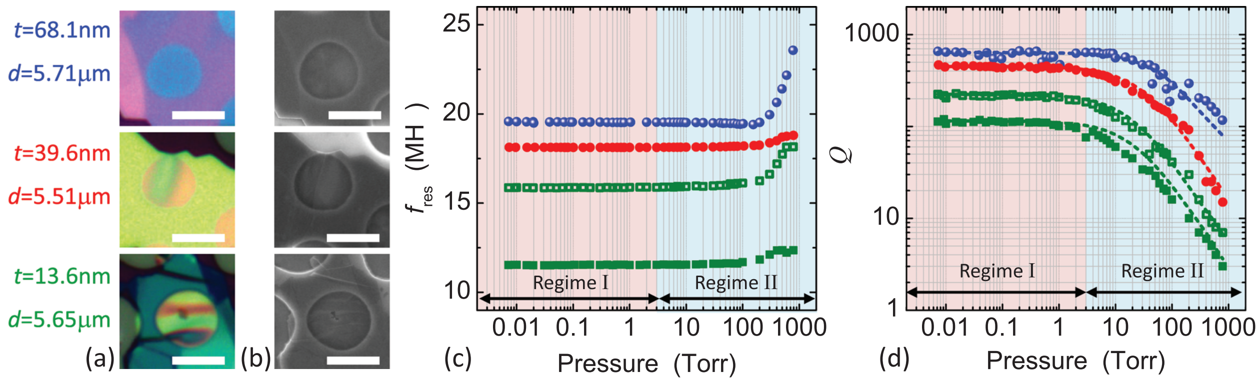

FIG. 4. Air damping in thick MoS_2 resonators. (a),(b) Optical and SEM images (scale bars: 5 μm). Devices dimensions labeled above images. (c) f_{res} and (d) Q as functions of p. Dashed lines are calculations using the FMF model. Symbol colors correspond to the colors of the device dimensions. Open symbols represent the second resonant mode of the $t = 13.6$ nm device.

dimensions and geometries. We find clear contrast in the pressure-dependent resonance behavior between 2D NEMS and conventional 3D MEMS resonators. Through analyzing the resonance data, we identify bulging-induced tensioning, compressing-cavity stiffening, and FMF damping in our MoS_2 resonators. By varying device thickness, we clearly observe effect of dimensionality in air damping behavior. Our results reveal possibilities toward exploiting different pressure dependences in 2D NEMS, for future applications including atomically thin tunable resonators, pressure sensing,[23] acoustic wave detection, and ultrasonic imaging.

We thank the support from Case School of Engineering, National Academy of Engineering (NAE) Grainger Foundation Frontier of Engineering (FOE) Award (FOE 2013-005) and CWRU Provost's ACES+ Advance Opportunity Award. Part of the device fabrication was performed at the Cornell NanoScale Facility (CNF), a member of the National Nanotechnology Infrastructure Network (NNIN), supported by the National Science Foundation (Grant No. ECCS-0335765).

[1]J. S. Bunch, A. M. van der Zande, S. S. Verbridge, I. W. Frank, D. M. Tanenbaum, J. M. Parpia, H. G. Craighead, and P. L. McEuen, Science **315**, 490–493 (2007).
[2]C. Chen, S. Rosenblatt, K. I. Bolotin, W. Kalb, P. Kim, I. Kymissis, H. L. Stormer, T. F. Heinz, and J. Hone, Nat. Nanotechnol. **4**, 861–867 (2009).
[3]A. M. van der Zande, R. A. Barton, J. S. Alden, C. S. Ruiz-Vargas, W. S. Whitney, P. H. Q. Pham, J. Park, J. M. Parpia, H. G. Craighead, and P. L. McEuen, Nano Lett. **10**, 4869–4873 (2010).
[4]C. Chen, S. Lee, V. V. Deshpande, G.-H. Lee, M. Lekas, K. Shepard, and J. Hone, Nat. Nanotechnol. **8**, 923–927 (2013).
[5]S. Shivaraman, R. A. Barton, X. Yu, J. Alden, L. Herman, M. V. S. Chandrashekhar, J. Park, P. L. McEuen, J. M. Parpia, H. G. Craighead, and M. G. Spencer, Nano Lett. **9**, 3100–3105 (2009).
[6]J. Lee, Z. Wang, K. He, J. Shan, and P. X.-L. Feng, ACS Nano **7**, 6086–6091 (2013).
[7]H. Tian, C. Li, M. A. Mohammad, Y.-L. Cui, W.-T. Mi, Y. Yang, D. Xie, and T.-L. Ren, ACS Nano **8**, 5883–5890 (2014).
[8]S. S. Verbridge, R. Ilic, H. G. Craighead, and J. M. Parpia, Appl. Phys. Lett. **93**, 013101 (2008).
[9]S. S. Verbridge, H. G. Craighead, and J. M. Parpia, Appl. Phys. Lett. **92**, 013112 (2008).
[10]D. M. Karabacak, V. Yakhot, and K. L. Ekinci, Phys. Rev. Lett. **98**, 254505 (2007).
[11]J. E. Sader, J. Appl. Phys. **84**, 64 (1998).
[12]S. Bianco, M. Cocuzza, S. Ferrero, E. Giuri, G. Piacenza, C. F. Pirri, A. Ricci, L. Scaltrito, D. Bich, A. Merialdo, P. Schina, and R. Correale, J. Vac. Sci. Technol. B **24**, 1803 (2006).
[13]O. Svitelskiy, V. Sauer, N. Liu, K.-M. Cheng, E. Finley, M. R. Freeman, and W. K. Hiebert, Phys. Rev. Lett. **103**, 244501 (2009).
[14]O. Ergincan, G. Palasantzas, and B. J. Kooi, Appl. Phys. Lett. **101**, 061908 (2012).
[15]Z. Kadar, W. Kindt, A. Bossche, and J. Mollinger, Sens. Actuators, A **53**, 299–303 (1996).
[16]D. R. Southworth, H. G. Craighead, and J. M. Parpia, Appl. Phys. Lett. **94**, 213506 (2009).
[17]J. S. Bunch, S. S. Verbridge, J. S. Alden, A. M. van der Zande, J. M. Parpia, H. G. Craighead, and P. L. McEuen, Nano Lett. **8**, 2458–2462 (2008).
[18]B. Ilic, S. Krylov, and H. G. Graighead, J. Appl. Phys. **107**, 034311 (2010).
[19]W. K. Schomburg, *Introduction to Microsystem Design* (Springer, New York, 2011), p. 50.
[20]W. E. Newell, Science **161**, 1320–1326 (1968).
[21]R. B. Bhiladvala and Z. J. Wang, Phys. Rev. E **69**, 036307 (2004).
[22]M. Bao and H. Yang, Sens. Actuators, A **136**, 3–27 (2007).
[23]J. Lee and P. X.-L. Feng, Proc. IEEE Int. Freq. Control Symp. (IFCS), Taipei, Taiwan, 19–22 May 2014, pp. 282–285.